Atmos. Meas. Tech., 15, 131–148, 2022
https://doi.org/10.5194/amt-15-131-2022

Atmospheric Measurement Techniques
Open Access
EGU

Inter-comparison of wind measurements in the atmospheric boundary layer and the lower troposphere with Aeolus and a ground-based coherent Doppler lidar network over China

Songhua Wu[1,2,3], Kangwen Sun[1], Guangyao Dai[1], Xiaoye Wang[1], Xiaoying Liu[1], Bingyi Liu[1,2], Xiaoquan Song[1,3], Oliver Reitebuch[4], Rongzhong Li[5], Jiaping Yin[5], and Xitao Wang[5]

[1]College of Marine Technology, Faculty of Information Science and Engineering, Ocean University of China, Qingdao, 266100, China
[2]Laboratory for Regional Oceanography and Numerical Modelling, Pilot National Laboratory for Marine Science and Technology (Qingdao), Qingdao, 266200, China
[3]Institute for Advanced Ocean Study, Ocean University of China, Qingdao, 266100, China
[4]Institute of Atmospheric Physics, German Aerospace Center (Deutsches Zentrum für Luft- und Raumfahrt e.V., DLR), 82234 Oberpfaffenhofen, Germany
[5]Qingdao Leice Transient Technology Co., Ltd., Qingdao, 266100, China

Correspondence: Songhua Wu (wush@ouc.edu.cn)

Received: 25 August 2021 – Discussion started: 27 August 2021
Revised: 30 October 2021 – Accepted: 24 November 2021 – Published: 5 January 2022

Abstract. After the successful launch of Aeolus, which is the first spaceborne wind lidar developed by the European Space Agency (ESA), on 22 August 2018, we deployed several ground-based coherent Doppler wind lidars (CDLs) to verify the wind observations from Aeolus. By the simultaneous wind measurements with CDLs at 17 stations over China, the Rayleigh-clear and Mie-cloudy horizontal-line-of-sight (HLOS) wind velocities from Aeolus in the atmospheric boundary layer and the lower troposphere are compared with those from CDLs. To ensure the quality of the measurement data from CDLs and Aeolus, strict quality controls are applied in this study. Overall, 52 simultaneous Mie-cloudy comparison pairs and 387 Rayleigh-clear comparison pairs from this campaign are acquired. All of the Aeolus-produced Level 2B (L2B) Mie-cloudy HLOS wind and Rayleigh-clear HLOS wind and CDL-produced HLOS wind are compared individually. For the inter-comparison result of Mie-cloudy HLOS wind and CDL-produced HLOS wind, the correlation coefficient, the standard deviation, the scaled mean absolute deviation (MAD) and the bias are 0.83, 3.15 m s^{-1}, 2.64 m s^{-1} and -0.25 m s^{-1}, respectively, while the $y = ax$ slope, the $y = ax + b$ slope and the $y = ax + b$ intercept are 0.93, 0.92 and -0.33 m s^{-1}. For the Rayleigh-clear HLOS wind, the correlation coefficient, the standard deviation, the scaled MAD and the bias are 0.62, 7.07 m s^{-1}, 5.77 m s^{-1} and -1.15 m s^{-1}, respectively, while the $y = ax$ slope, the $y = ax + b$ slope and the $y = ax + b$ intercept are 1.00, 0.96 and -1.2 m s^{-1}. It is found that the standard deviation, the scaled MAD and the bias on ascending tracks are lower than those on descending tracks. Moreover, to evaluate the accuracy of Aeolus HLOS wind measurements under different product baselines, the Aeolus L2B Mie-cloudy HLOS wind data and L2B Rayleigh-clear HLOS wind data under Baselines 07 and 08, Baselines 09 and 10, and Baseline 11 are compared against the CDL-retrieved HLOS wind data separately. From the comparison results, marked misfits between the wind data from Aeolus Baselines 07 and 08 and wind data from CDLs in the atmospheric boundary layer and the lower troposphere are found. With the continuous calibration and validation and product processor updates, the performances of Aeolus wind measurements under Baselines 09 and 10 and Baseline 11 are improved significantly. Considering the influence of turbulence and convection in the atmospheric boundary layers and the lower troposphere, higher values for the vertical velocity are common in this region.

Published by Copernicus Publications on behalf of the European Geosciences Union.

Hence, as a special note, the vertical velocity could impact the HLOS wind velocity retrieval from Aeolus.

1 Introduction

Reliable instantaneous vertical profiling of the global wind field, especially over the tropics and oceans, is crucial to many aspects of climate change, oceanography research, large-scale weather systems and weather prediction. It is also needed to address some of the key concerns of atmospheric dynamics and climate processes (Stoffelen et al., 2005). The wind field measurements are important for studies of the large-scale monsoon systems and El Niño phenomenon in tropics and the jet stream in extra-tropics. Wind profiles are available from the global radiosonde network and aircraft ascents and descents and cruising altitudes for numerical weather prediction (Zhang et al., 2020; Guo et al., 2021a). However, due to the lack of wind profiles over ocean areas from the radiosonde network and wind observations only at a specific flight altitude (around 10–12 km about ground level) in aircraft measurements, a first-ever spaceborne direct-detection wind lidar, Aeolus, which is capable of providing the globally high spatial and temporal vertical wind profiles, was developed by the European Space Agency (ESA) under the framework of the Atmospheric Dynamics Mission (Stoffelen et al., 2005; ESA, 1999; Reitebuch, 2012). On 22 August 2018, Aeolus was successfully launched into its sun-synchronous orbit at a height of 320 km (Kanitz et al., 2018; Straume et al., 2018; Reitebuch et al., 2020). A quasi-global coverage is achieved daily ($\sim$ 16 orbits per day), and the orbit repeat cycle is 7 d (111 orbits). The orbit is sun-synchronous, with a local equatorial crossing-time of 06:00 and 18:00 local time (LT). The Atmospheric Laser Doppler Instrument (ALADIN) is a direct-detection high-spectral-resolution wind lidar operating at a laser wavelength of 354.8 nm and provides vertical profiles of the line-of-sight (LOS) wind speed. In order to retrieve the LOS wind speeds, the Doppler shifts in light caused by the motion of molecules and aerosol particles need to be identified. Aiming at this, a Fizeau interferometer is applied in the Mie channel to extract the frequency shift in the narrow-band particulate return signal by means of a fringe imaging technique (Mckay, 2002). In the Rayleigh channel, two coupled Fabry–Pérot interferometers are used to analyse the frequency shift in the broad-band molecular return signal by the double-edge technique (Chanin et al., 1989; Flesia and Korb, 1999).

After the successful launch of ALADIN, the data products were released to the Aeolus Cal/Val teams on 16 December 2018. To recheck the quality of the data products, a validation of Aeolus winds by means of ground-based, airborne and shipborne reference instrument measurements is inevitable. From the validation campaigns conducted by the German Aerospace Center (Deutsches Zentrum für Luft- und Raumfahrt e.V., DLR), the wind observations from Aeolus and the well-validated ALADIN Airborne Demonstrator (A2D) are compared (Lux et al., 2020a; Witschas et al., 2020). An example of early validation of Aeolus with a direct-detection Rayleigh–Mie Doppler lidar was performed at the Observatoire de Haute-Provence (OHP) in southern France (Khaykin et al., 2020). In November and December 2018, a unique validation of the wind products of Aeolus in the Atlantic Ocean west of the African continent was conducted by using the radiosondes carried on RV *Polarstern* cruise PS116 (Baars et al., 2020). In China, the wind observations from Aeolus were compared with the results from the ground-based radar wind profiler network and radiosondes (Guo et al., 2021b). There were some significant validation campaigns as well using airborne instruments and radiosondes (e.g. Bedka et al., 2021; Martin et al., 2021).

As a member of the Cal/Val teams, the Ocean University of China (OUC) has performed one long-term observation campaign with 1550 nm coherent Doppler wind lidars (CDLs) all over China. During the campaign, 439 simultaneous measurement cases were acquired with the CDLs of types Wind3D 6000 and WindMast PBL, which are manufactured by Qingdao Leice Transient Technology Co., Ltd (http://www.leice-lidar.com/en/index.html, last access: 23 August 2021). During the data processing, it was found that the atmospheric vertical velocity could influence the horizontal-line-of-sight (HLOS) wind velocity measured by Aeolus in the atmospheric boundary layer and the lower troposphere. Hence, it should be specially noted that the HLOS wind velocities from CDLs and Aeolus are different and should be corrected.

This paper provides the inter-comparison of the HLOS wind velocities measured by CDLs and Aeolus. The paper is organized as follows: in Sect. 2 the simultaneous validation campaigns and the instrument deployed for the measurements are described. Section 3 presents the details to the inter-comparison strategy, the quality control and vertical-velocity-correction procedure. In Sect. 4 we provide the HLOS wind velocity measurement examples and comparison results. Section 5 summarizes the recent comparison results and compares those with ours.

2 Validation campaigns in China and lidar introduction

2.1 Overview of the validation campaigns

Shortly after the successful launch of the Aeolus, the primary laser head FM-A (flight model laser A) was switched on, and an initial laser pulse energy of 65 mJ was achieved (Lux et al., 2020b). During the period from 14 January to 14 February 2019, Aeolus was in standby mode and switched on with FM-A. After a final test with laser FM-A of Aeolus on 17 June, the transition to laser FM-B took place. About half a year later, beginning in January 2020, the validation

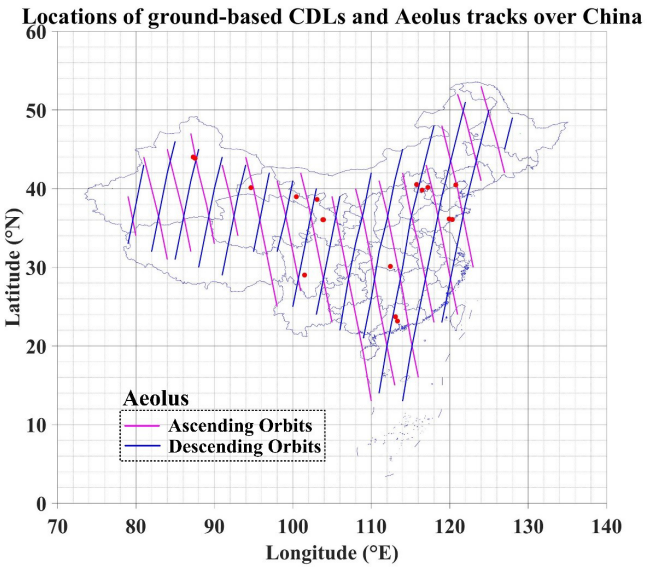

Figure 1. Ground-based CDL observation sites of the VAL-OUC campaign since January 2020. The pink and blue swaths indicate the ascending and descending orbits of Aeolus. The red dots represent the locations of the CDLs.

campaign (VAL-OUC) performed by the Ocean University of China was carried out at 17 stations. The comparison results of HLOS wind velocities in the atmospheric boundary layer and the lower troposphere from CDLs and Aeolus are presented in Sect. 4. The duration of the validation campaign (VAL-OUC) was from January to December 2020. The locations of the CDLs and the ascending and descending orbits of Aeolus are shown in Fig. 1. An overview and detailed information of the validation campaign are provided in Table 1.

2.2 The ALADIN and CDL descriptions

In this subsection, the unique payload of Aeolus, the Atmospheric Laser Doppler Instrument (ALADIN), and the ground-based reference coherent Doppler wind lidar are briefly described.

2.2.1 ALADIN

ALADIN is a direct-detection high-spectral-resolution wind lidar which operates at a wavelength of 354.8 nm, with a laser pulse energy around 65 mJ and with a repetition of 50.5 Hz (Lux et al., 2020b). It is equipped with a 1.5 m diameter telescope to collect the backscatter light from molecules and aerosol particles. The high-spectral-resolution design of ALADIN allows for the simultaneous detection of the molecular (Rayleigh) and particle (Mie) backscattered signals in two separate channels, each sampling the wind in 24 vertical height bins with a vertical range resolution between 0.25 and 2.0 km. This makes it possible to deliver winds in both clear and (partly) cloudy conditions down to optically thick clouds at the same time. The horizontal resolution of the wind observations is about 90 km for the Rayleigh channel and about 10–15 km for the Mie channel. A detailed description of the instrument design and a demonstration of the measurement concept are introduced in, for example, Reitebuch et al. (2009), Reitebuch (2012), Straume et al. (2018), ESA (2008) and Marksteiner (2013).

The data products of Aeolus are processed at different levels mainly including Level 0 (instrument housekeeping data), Level 1B (engineering-corrected HLOS winds), Level 2A (aerosol and cloud layer optical properties), Level 2B (meteorologically representative HLOS winds) and Level 2C (Aeolus-assisted wind vectors from the ECMWF model) (Tan et al., 2008; Rennie and Isaksen, 2020). In this study, the Level 2B HLOS wind velocities are used. Within the Level 2B processor, the Rayleigh-clear and Mie-cloudy winds are classified, and the temperature and pressure correction are applied for the Rayleigh wind retrieval.

2.2.2 Coherent Doppler wind lidar instrument

Lidar is one of the most accurate optical remote sensing techniques for wind field measurements. The 1550 nm wavelength all-fibre coherent Doppler wind lidar (CDL) with high resolution takes advantage of the fact that the frequency of the echo signal is shifted from the local-oscillator light because of the Doppler effect, which occurs from backscattering of aerosols. The Doppler frequency shift in the backscattered signal is analysed to obtain the LOS velocity along the lidar beam direction. The CDL is based on the heterodyne technique, consisting of a single-frequency seed laser source, an acousto-optic modulator, an erbium-doped fibre amplifier, optical isolators, amplified spontaneous emission noise filters, an optical switch, a transceiver telescope, a balanced detector, an analogue-to-digital converter and a fast Fourier transform signal processor. Further information regarding the CDL is described in a separate paper (Wu et al., 2016).

The CDLs of types Wind3D 6000 and WindMast PBL are lidar systems for wind measurements in the lower atmosphere. The devices were developed by Qingdao Leice Transient Technology Co., Ltd. and designed with consideration of the needs of the meteorological application, wind energy industry and aviation safety. The specifications of the CDLs are listed in Table 2.

To evaluate the accuracy and precision of ground-based CDL measurements, the Wind3D 6000 and the WindMast PBL were validated with mast-mounted cup anemometers and wind vanes at Haiyang, Shandong Province, of China from 23 to 30 July 2021. The photos of the CDLs and the mast onto which the cup anemometers and the wind vines were mounted at the Haiyang site are shown in Fig. 2. The horizontal distance between the Wind3D 6000, the WindMast PBL and the mast is around 6 m. The met mast configuration is compliant with International Electrical Commission (IEC) 61400-12-1 Edition 2 (IEC, 2011). All cup anemome-

Table 1. Overview of Aeolus validation campaigns performed by the OUC.

Validation campaigns	Instrument type	Measurement mode	Location	Latitude, longitude, altitude	Measurement period
VAL-OUC	WindMast PBL	DBS*	Dunhuang	40.12° N, 94.66° E; 1.15 km	From 7 Jan to 29 Dec 2020
	WindMast PBL	DBS	Lanzhou	36.05° N, 103.91° E; 1.51 km	From 7 Jan to 29 Dec 2020
	WindMast PBL	DBS	Zhangye	38.97° N, 100.45° E; 1.46 km	From 5 Jan to 27 Dec 2020
	Wind3D 6000	DBS	Jingzhou	30.11° N, 112.44° E; 0.03 km	From 24 Jun to 22 Jul 2020
	Wind3D 6000	DBS	Pinggu, Beijing	40.15° N, 117.22° E; 0.05 km	From 21 Apr to 2 Jun 2020
	Wind3D 6000	DBS	Changji	44.01° N, 87.30° E; 0.58 km	3 Dec 2020
	Wind3D 6000	DBS	Jiulong, Sichuan	29.01° N, 101.50° E; 2.90 km	From 24 Oct to 29 Nov 2020
	Wind3D 6000	DBS	Jiaozhou, Shandong	36.14° N, 119.93° E; 0.02 km	21 Dec 2020
	Wind3D 6000	DBS	Qingyuan, Guangdong	23.71° N, 113.09° E; 0.03 km	From 12 May to 27 Aug 2020
	Wind3D 6000	DBS	Xidazhuangke, Beijing	40.52° N, 115.78° E; 0.91 km	From 7 Jan to 31 Mar 2020
	Wind3D 6000	DBS	Yizhuang, Beijing	39.81° N, 116.48° E; 0.04 km	From 7 Apr to 25 Aug 2020
	Wind3D 6000	DBS	Huludao	40.47° N, 120.78° E; 0.10 km	From 1 Nov to 28 Dec 2020
	Wind3D 6000	DBS	Wuwei	38.62° N, 103.09° E; 1.37 km	From 11 Apr to 26 Dec 2020
	Wind3D 6000	DBS	Lanzhou	36.05° N, 103.83° E; 1.53 km	From 4 Jan to 26 Dec 2020
	Wind3D 6000	DBS	South China University of Technology	23.16° N, 113.34° E; 0.03 km	From 13 Oct to 29 Dec 2020
	Wind3D 6000	DBS	Ürümqi	43.85° N, 87.55° E; 0.84 km	From 14 Oct to 24 Dec 2020
	Wind3D 6000	DBS	Qingdao	36.07° N, 120.34° E; 0.04 km	From 2 Nov to 28 Dec 2020

* DBS: Doppler beam swinging.

ters installed on the reference mast are class 0.9A instruments and have undergone individual rotor-specific MEASNET calibration at a MEASNET-certified wind tunnel. Data acquisition systems sample all input ports and connected sensors continuously with a sampling rate of 1 Hz and compress the values to 10 min average values. The specifications of the cup anemometers and wind vanes are listed in Table 3. The measurement heights selected for comparison are 50 and 100 m. Figure 3 shows the comparison results at 50 m, which are wind speed and wind direction for Wind3D 6000 and WindMast PBL, respectively. By performing ordinary-least-squares linear regressions of the CDLs, cup anemometers and wind vine wind measurements, the slopes, offsets, standard deviations and correlation coefficients are acquired, and they are within the acceptable limits. The statistic results of the validation are shown in Table 4. Hence, the CDLs of

Table 2. Overview of CDL specifications used for Aeolus validation.

Qualification	Specifications	
	Wind3D 6000	WindMast PBL
Wavelength	1550 nm	1550 nm
Repetition rate	10 kHz	10 kHz
Pulse energy	160 µJ	100 µJ
Pulse width	100 to 400 ns	100 to 400 ns
Detection range	80 to 6000 m	30 to 4000 m
Data update rate	4 Hz	4 Hz
Range resolution	15 to 60 m	15 to 30 m
Wind speed accuracy	$\leq 0.1\,\mathrm{m\,s^{-1}}$	$\leq 0.1\,\mathrm{m\,s^{-1}}$
Wind speed range	$\pm 75\,\mathrm{m\,s^{-1}}$	$\pm 75\,\mathrm{m\,s^{-1}}$
Wind direction accuracy	0.1°	0.1°

types Wind3D 6000 and WindMast PBL can act as reference instruments for the validation of Aeolus in the atmospheric boundary layer and the lower troposphere.

3 Inter-comparison of Aeolus and CDL measurements

During the validation campaigns of VAL-OUC, the wind field measurements at the sites over China are continuously performed, except during the period of the CDL maintenances.

3.1 Inter-comparison strategy

In Fig. 4, we provide the flowchart of the comparison between Wind3D 6000 and WindMast PBL measurements against Aeolus measurements. To ensure the quality of the measurement data from Wind3D 6000 and WindMast PBL, we only used the CDL data with a signal-to-noise ratio (SNR) of > -10 dB. For Aeolus, only observations with the corresponding "validity_flag" of TRUE, which is provided in the Aeolus Level 2B (L2B) product, are considered. For the comparison, only the Mie-cloudy and Rayleigh-clear wind velocities from the L2B product with estimated errors lower than 4 and $8\,\mathrm{m\,s^{-1}}$, respectively, are selected (Witschas et al., 2020). Moreover, the Aeolus lowest-atmospheric-range bins close to the ground are also removed from the comparison because the lowest-atmospheric-range bins from Aeolus could be contaminated by the ground. In this study, the horizontal separations between the locations of CDLs and the Aeolus measurement ground track should be less than 80 km. Since the CDLs provide continuous atmospheric observations, there is no time difference between CDLs and simultaneous Aeolus measurements. Vertical averaging of the CDL measurements over one Aeolus range bin is also performed.

To observe the three-dimensional wind speed and direction, the Doppler beam swing (DBS) scanning mode of CDLs is applied. The five-beam DBS scanning technique is mainly used to retrieve the wind profiles by measuring the LOS wind speeds in the vertical, the northern, the eastern, the southern and the western directions. The original wind product of CDLs is 1 s average results (Level 2 product). By considering the low horizontal spatial resolution of Aeolus data (about 90 km for the Rayleigh-clear wind velocities and 10 km for the Mie-cloudy wind velocities), a 30 min (±15 min) average of the CDL wind product is applied, and the nearest observation profile provided by CDLs and Aeolus is selected by using the geolocation information in each measurement case. Since Aeolus can only deliver the HLOS wind data, the simultaneous wind measurements from CDLs have to be projected onto the Aeolus HLOS wind direction using the azimuth angle from Aeolus. The CDL-HLOS wind ($\mathrm{HLOS_{CDL}}$) is calculated as

$$\mathrm{HLOS_{CDL}} = V_{\text{CDL-EW}} \cdot \sin(\mathrm{Azi_{Aeolus}}) + V_{\text{CDL-SN}} \cdot \cos(\mathrm{Azi_{Aeolus}}). \quad (1)$$

$V_{\text{CDL-EW}}$ and $V_{\text{CDL-SN}}$ are the east–west wind speed and the south–north wind speed measured by CDLs, respectively, and $\mathrm{Azi_{Aeolus}}$ is the azimuth angle of ALADIN provided with the Aeolus products.

3.2 Influence of vertical velocity in the atmospheric boundary layer and the lower troposphere

In the atmospheric boundary layer and the lower troposphere, the vertical velocity of air mass shows a pronounced impact on the HLOS wind velocity measured by Aeolus. The schematic diagram of the vertical velocity impacts on the HLOS wind velocity retrieval is presented in Fig. 5. Hence, the difference between the HLOS wind velocities from CDLs and Aeolus should be specially treated for the comparison.

As shown in Fig. 5, the off-nadir angle of ALADIN is 35°. Because of the curvature of the earth's surface, the viewing angle of the laser beam from ground becomes 37°, which is used in the vertical velocity correction. According to the projection relationship, the LOS component of vertical velocity is $V_1 = V_{\text{vertical}} \cdot \cos 37°$. Resulting from the definition of Aeolus HLOS wind ($V_{\text{HLOS}} = V_{\text{LOS}} / \sin 37°$), the influence of V_1 on V_{HLOS} is $V_2 = V_1 / \sin 37°$. Consequently, the influence of V_{vertical} on V_{HLOS} is $V_2 = V_{\text{vertical}} \cdot \cos 37° / \sin 37°$, i.e. $V_2 = V_{\text{vertical}} \cdot \cot 37°$.

Thus, the relationship between $\mathrm{HLOS_{CDL}}$ and $\mathrm{HLOS_{Aeolus}}$ should be expressed as

$$\mathrm{HLOS_{Aeolus}} = \mathrm{HLOS_{CDL}} + V_{\text{vertical}} \cot 37°. \quad (2)$$

$\mathrm{HLOS_{Aeolus}}$ is calculated from the LOS wind (V_1 in Fig. 5) by the projection relationship. It not only includes the information of horizontal wind field but is also influenced by the vertical speed. As introduced in Sect. 3.1, $\mathrm{HLOS_{CDL}}$ is decided only by the horizontal wind field measured by CDLs.

Figure 2. Photos of the CDLs and the mast onto which the cup anemometers and the wind vines were mounted at the Haiyang site.

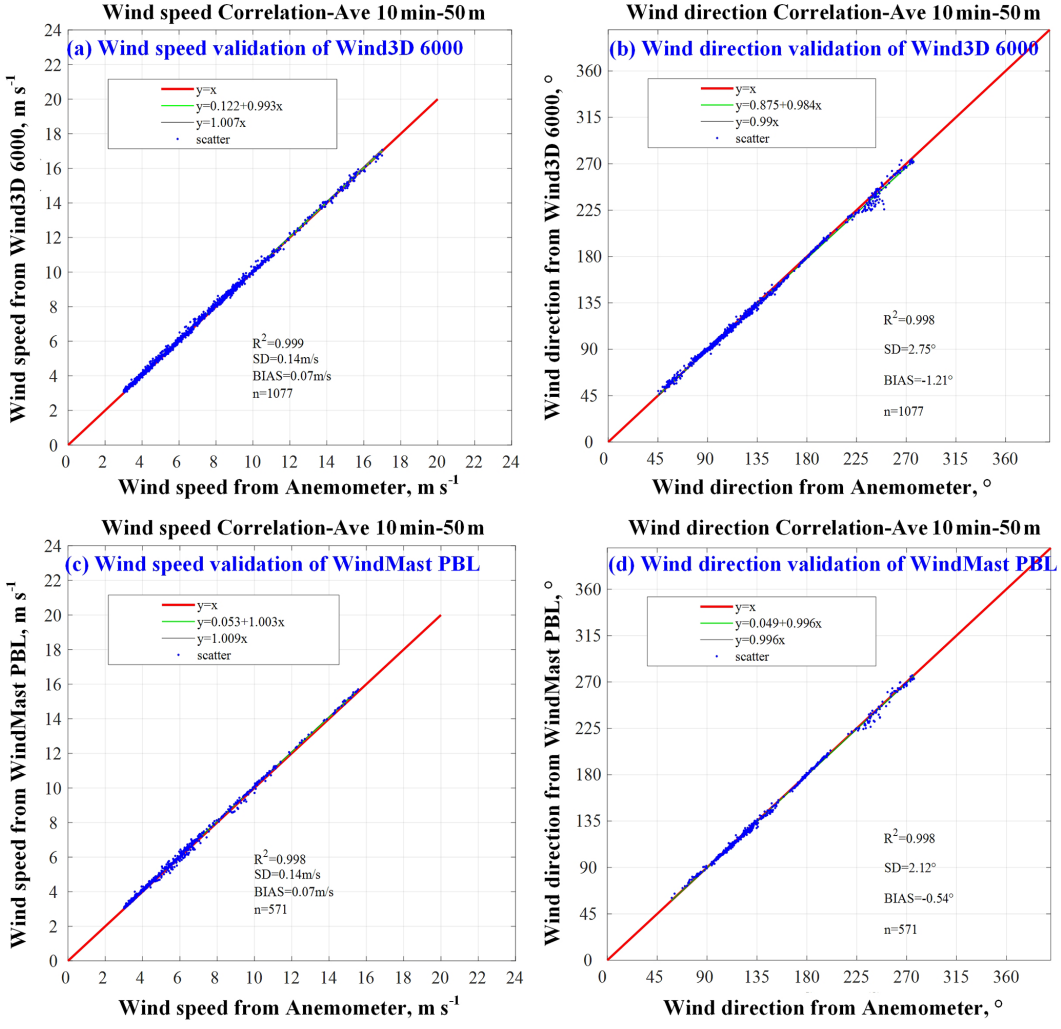

Figure 3. Evaluation tests of **(a, b)** Wind3D 6000 and **(c, d)** WindMast PBL performance by comparing their measurements against the conventional wind measurements with mast-mounted cup anemometers and wind vanes.

Table 3. Overview of the specifications of cup anemometers and wind vanes used for CDL validation.

Name of instrument	Type	Accuracy	Sampling frequency	Height
WS_50m_E	First Class Advanced 4.3351.00.000	$0.2\,m\,s^{-1}$	1 Hz	50 m
WS_50m_F	First Class Advanced 4.3351.00.000	$0.2\,m\,s^{-1}$	1 Hz	50 m
WD_48m	First Class Vane 4.3151.00.173	1°	1 Hz	48 m

Table 4. Statistical results of the validation tests between Wind3D 6000, WindMast PBL and cup anemometers, and wind vines.

Specifications	Wind speed from Wind3D 6000	Wind direction from Wind3D 6000	Wind speed from WindMast PBL	Wind direction from WindMast PBL
N points	1077	1077	571	571
Correlation	0.999	0.998	0.998	0.998
SD	0.14 ($m\,s^{-1}$)	2.75 (°)	0.14 ($m\,s^{-1}$)	2.12 (°)
BIAS	0.07 ($m\,s^{-1}$)	−1.21 (°)	0.07 ($m\,s^{-1}$)	−0.54 (°)
$y = ax$ slope	1.007	0.99	1.009	0.996
$y = ax + b$ slope	0.993	0.984	1.003	0.996
$y = ax + b$ intercept	0.122 ($m\,s^{-1}$)	0.875 (°)	0.053 ($m\,s^{-1}$)	0.049 (°)

Vertical wind measurements in the atmospheric boundary layer and the lower troposphere during the validation campaigns at each site are performed. In Fig. 6, one vertical-wind-measurement case with a moving average of 30 min is provided. From this figure, it is found that the typical temporal average of vertical wind is ±0 to $\pm 0.40\ m\,s^{-1}$. According to the schematic diagram of the vertical velocity impact plotted in Fig. 5, the vertical wind with a speed of $\pm 0.40\,m\,s^{-1}$ will introduce an error of up to $\pm 0.53\,m\,s^{-1}$ in retrieving HLOS wind. The maximum and minimum vertical velocities are up to around 1 and $-1\,m\,s^{-1}$, which could introduce errors of $\pm 1.33\,m\,s^{-1}$, respectively. Thus, the HLOS wind from CDLs is corrected considering the vertical velocity effect. In Figs. 7 and 8, the CDL V_w correction (30 min) profiles (yellow lines) are the corrected results by the vertical velocity correction. It should be emphasized that, because of the horizontal distances between the Aeolus scanning tracks and the ground-based CDL sites as well as the heterogeneous atmospheric boundary layer, the vertical velocity correction is only used in the profile analysis for the method discussion, and the corrected CDL HLOS wind results are not used in the statistical comparison.

4 Results and analyses

In the validation campaign, the CDLs of types Wind3D 6000 and WindMast PBL are deployed at different observations sites. According to the sketch illustrated in Fig. 4, the measurement data from CDLs and Aeolus are processed. In this section, some examples of single profiles and a statistical analysis are presented.

4.1 Profile comparison

To compare the measurement results in Qingdao, the simultaneous profiles of HLOS wind velocities observed with Aeolus and Wind3D 6000 are provided in Fig. 7. Firstly, it should be introduced that the Aeolus L2B data of this case were produced by the processor Baseline 11. In this figure, the CDL-retrieved HLOS wind velocities with and without vertical velocity correction are compared against the Aeolus Mie L2B products and Rayleigh L2B products. The vertical velocity profile is plotted as well. From this figure, it is found that the Aeolus L2B Rayleigh-clear HLOS wind profile in the atmospheric boundary layer and the lower troposphere is almost trustable, except for the lowest height bin of the Aeolus Rayleigh-clear HLOS wind profile, which has a large bias compared with the CDL-retrieved HLOS wind. In the aspect of the Aeolus L2B Mie-cloudy HLOS wind profile, in the atmospheric boundary layer and the lower troposphere, the synchronous CDL measurements are in the range of the estimated error provided in the Aeolus L2B product. Additionally, the 30 min averaged vertical velocity profile shows that the vertical velocity is in the range of $\pm 0.30\,m\,s^{-1}$, which could introduce the error range of around $\pm 0.40\,m\,s^{-1}$ according to the method provided in Sect. 3.2.

To compare the measurement results, four simultaneous profiles of HLOS wind velocities observed with Aeolus and CDLs on 21 January, 11 April, 18 September and 15 November 2020 (UTC) at Xidazhuangke (Beijing), Lanzhou (Gansu Province), Wuwei (Gansu Province) and Huludao (Liaoning Province) are shown in Fig. 8. In this figure, the CDL-retrieved HLOS wind velocities with and without vertical velocity correction are compared against the Aeolus L2B Mie-cloudy products and Rayleigh-clear HLOS wind prod-

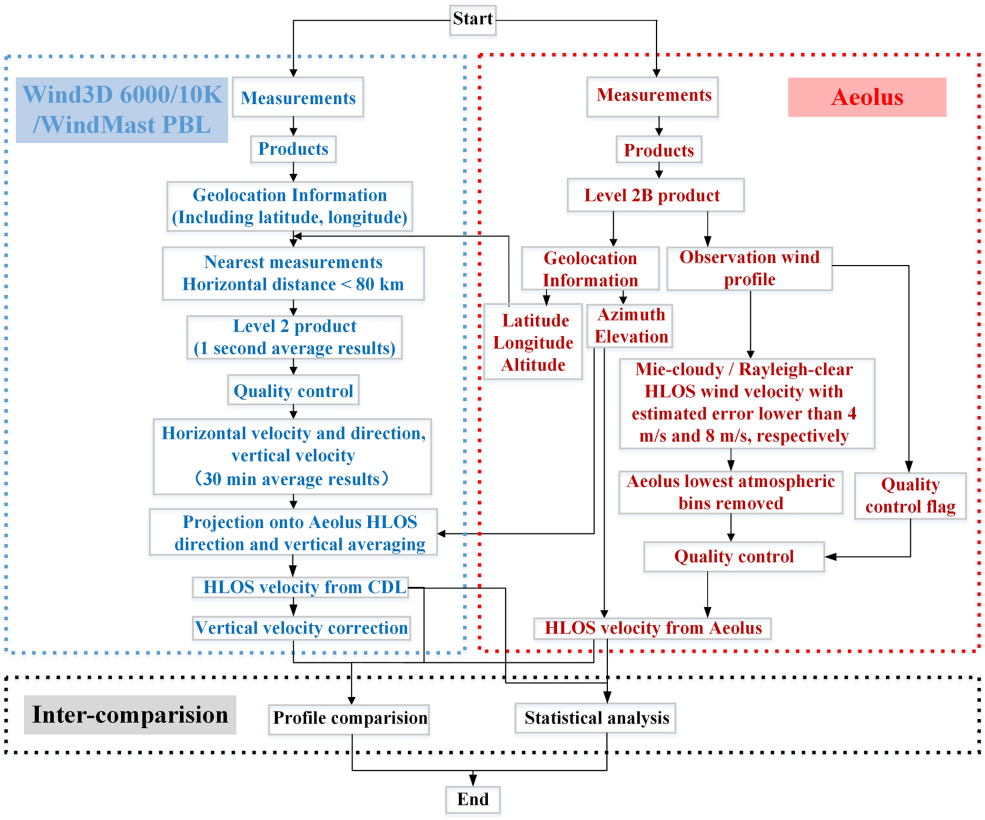

Figure 4. Sketch of the comparison between CDLs and Aeolus in the atmospheric boundary layer and the lower troposphere.

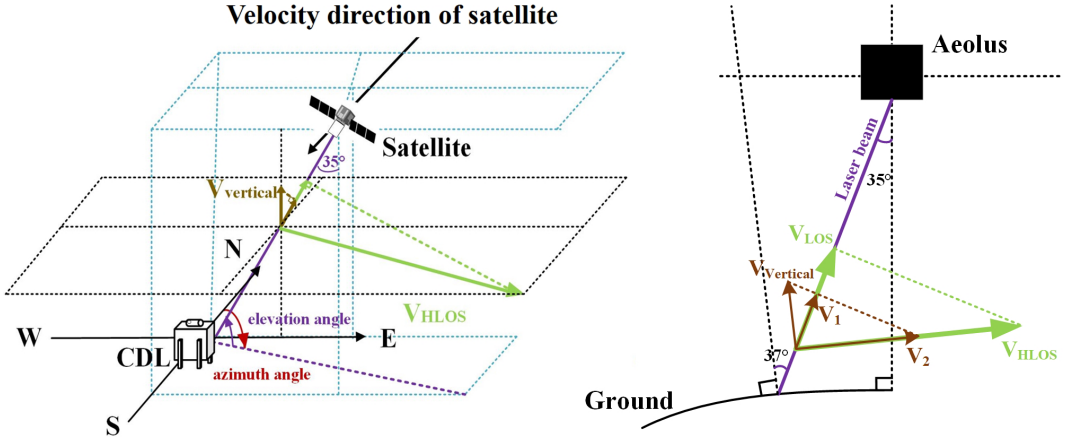

Figure 5. The schematic diagram of the vertical velocity impact on the HLOS wind velocity retrieval of Aeolus.

ucts. The vertical velocity profiles are shown as well. From Fig. 8a, it is found that the Aeolus L2B Mie-cloudy products in the atmospheric boundary layer and the lower troposphere fit well with the CDL-retrieved HLOS wind velocities. In Fig. 8b, c and d, the CDL-retrieved HLOS wind velocities and the Aeolus L2B Rayleigh-clear HLOS wind products agree well from the atmospheric boundary layer to the altitude of around 6 km, while the CDL-retrieved profiles are all in the range of the estimated errors provided in the Aeolus L2B products. It should be emphasized that the Xidazhuangke (Beijing) case uses the Aeolus L2B HLOS wind data on 21 January, which are from Baseline 07, while the processor of the Aeolus data in the Lanzhou (Gansu Province) case on 11 April is Baseline 08, and the processors of the Aeolus data in the Wuwei (Gansu Province) case and Huludao (Liaoning Province) case on 18 September and

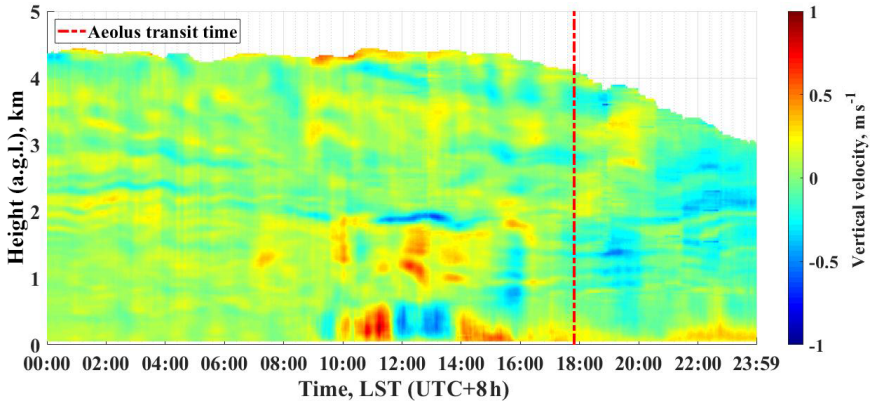

Figure 6. Vertical velocity (moving average of 30 min) measured on 16 November 2020 in Qingdao (Shandong Province), China. The dashed red line indicates the Aeolus transit time.

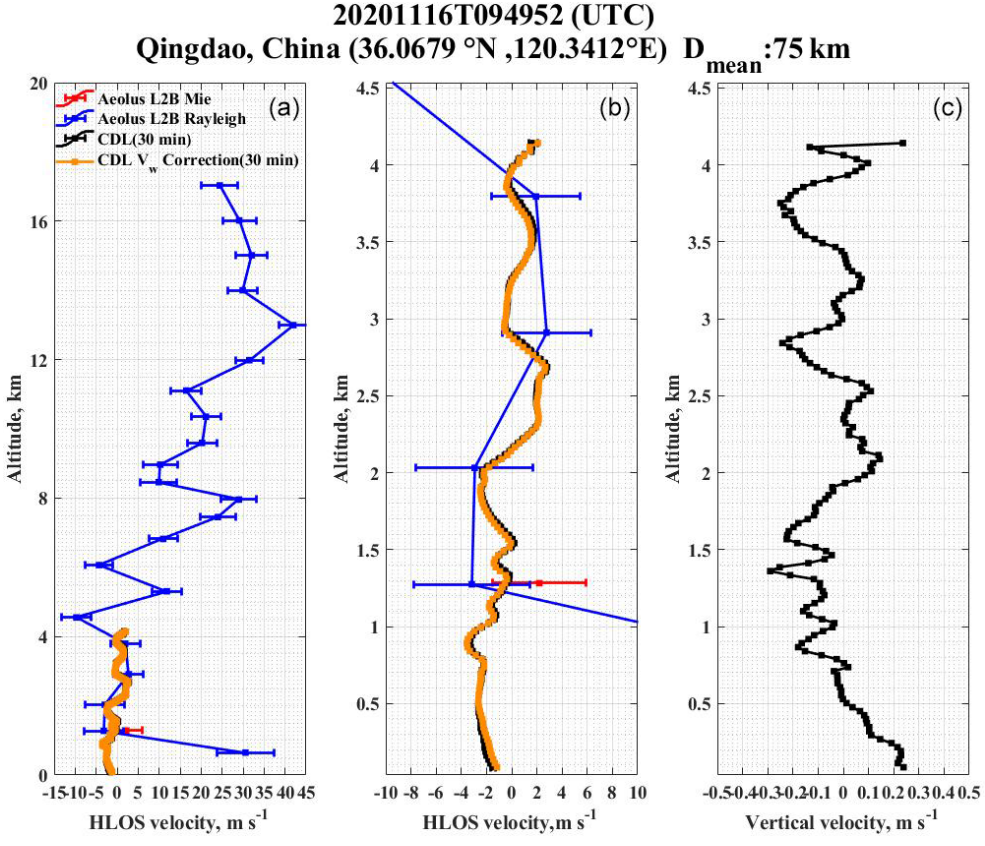

Figure 7. Inter-comparison of HLOS wind velocities measured with CDLs and Aeolus on 16 November 2020 at Qingdao (Shandong Province), China. Panel **(a)** is the overall view of the inter-comparison result, where the red line represents the Aeolus L2B Mie-cloudy HLOS wind profile, the blue line represents the Aeolus L2B Rayleigh-clear HLOS wind profile, the black line represents the CDL-retrieved HLOS wind profile, and the yellow line represents the vertical-velocity-corrected CDL-retrieved HLOS wind profile. Panel **(b)** shows the partial view of the inter-comparison result; the lines are the same as panel **(a)**. Panel **(c)** is the vertical velocity profile.

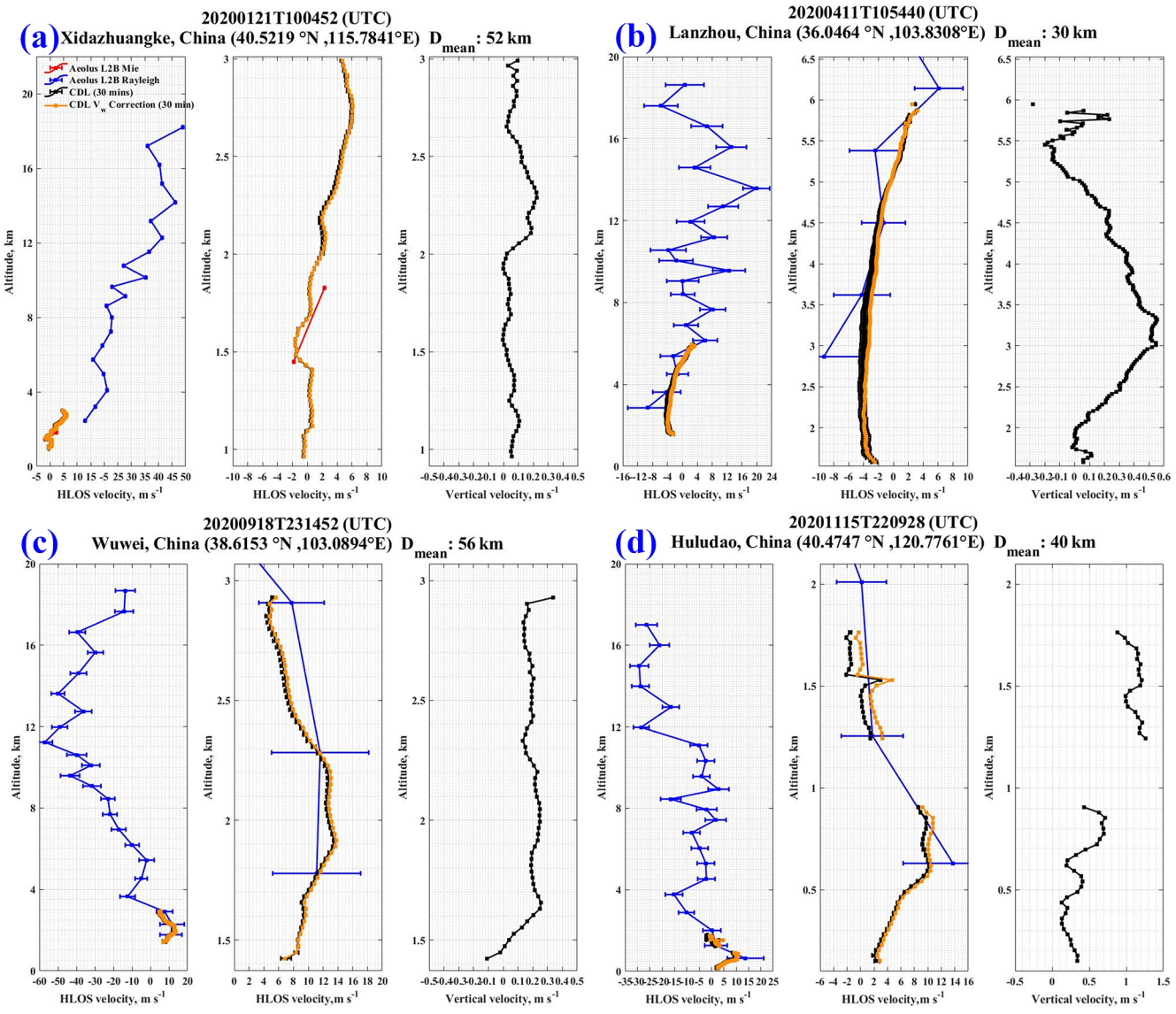

Figure 8. Inter-comparison of HLOS wind velocities measured with CDLs and Aeolus at **(a)** Xidazhuangke (Beijing), **(b)** Lanzhou (Gansu Province), **(c)** Wuwei (Gansu Province) and **(d)** Huludao (Liaoning Province) on 21 January, 11 April, 18 September and 15 November 2020, respectively. The lines are the same as those of Fig. 7.

15 November are Baseline 10 and Baseline 11, respectively. It is because the adaptive bias correction based on ECMWF data and the M1 telescope temperatures, which was added after Baseline 09 was not yet in place for Baseline 07, that there is the noticeable bias for the Rayleigh channel winds in the Xidazhuangke (Beijing) case (Rennie et al., 2020; Weiler et al., 2021). Besides, in the inter-comparison case of Huludao (Fig. 8d), in the altitude of around 1.2 to 1.7 km, the vertical velocity measured by CDLs is larger than 1.00 m s^{-1}, which could introduce an error of about 1.33 m s^{-1} if it is not considered. The vertical-velocity-corrected results (the yellow line) show the better agreement with the Aeolus L2B Rayleigh-clear HLOS wind velocities than the original CDL-retrieved HLOS wind velocities.

4.2 Statistical comparison

In this section, we compare the HLOS wind velocity results from Aeolus observations with the accompanying ground-based CDL measurements. During the time period of January to December 2020 within the VAL-OUC campaign, 52 simultaneous Mie-cloudy comparison pairs and 387 Rayleigh-clear comparison pairs at 17 stations are acquired. Figure 9 shows the numbers of the comparison data pairs at different detection height ranges of the Mie-cloudy channel and Rayleigh-clear channel. It can be seen that the heights of the

Table 5. Statistical comparison of Aeolus HLOS winds and CDL-retrieved HLOS winds.

Channel	Mie-cloudy	Rayleigh-clear
N points	52	387
Correlation	0.83	0.62
SD ($m\,s^{-1}$)	3.15	7.07
Scaled MAD ($m\,s^{-1}$)	2.64	5.77
BIAS ($m\,s^{-1}$)	−0.25	−1.15
$y = ax$ slope	0.93	1.00
$y = ax + b$ slope	0.92	0.96
$y = ax + b$ intercept ($m\,s^{-1}$)	−0.33	−1.20

Table 6. Statistical comparison of Aeolus Rayleigh ascending and descending HLOS winds and CDL-retrieved HLOS winds.

Ascending and descending	Ascending	Descending
N points	127	254
Correlation	0.65	0.51
SD ($m\,s^{-1}$)	5.83	7.47
Scaled MAD ($m\,s^{-1}$)	4.90	6.06
BIAS ($m\,s^{-1}$)	−0.16	−2.00
$y = ax$ slope	1.02	0.97
$y = ax + b$ slope	1.03	0.78
$y = ax + b$ intercept ($m\,s^{-1}$)	−0.23	−2.61

comparison pairs are mainly in and close to the atmospheric boundary layer and the lower troposphere.

In Fig. 10, the Mie-cloudy HLOS wind velocities and Rayleigh-clear HLOS wind velocities from Aeolus are compared with those from CDLs, respectively. Figure 10a presents the scatter diagram of Aeolus L2B Mie-cloudy HLOS wind and CDL HLOS wind. A total of 52 measurement cases for Mie-cloudy winds are available for the comparison. From this result, the correlation coefficient, the standard deviation, the scaled mean absolute deviation (MAD) and the bias are 0.83, 3.15 $m\,s^{-1}$, 2.64 $m\,s^{-1}$ and −0.25 $m\,s^{-1}$, respectively, while the $y = ax$ slope, $y = ax + b$ slope and $y = ax + b$ intercept are 0.93, 0.92 and −0.33 $m\,s^{-1}$. In Fig. 10c, the scatter diagram of Aeolus L2B Rayleigh-clear HLOS wind and CDL HLOS wind data is plotted. There are 387 comparisons taken into consideration. Accordingly, the correlation coefficient, the standard deviation, the scaled MAD and the bias are 0.62, 7.07 $m\,s^{-1}$, 5.77 $m\,s^{-1}$ and −1.15 $m\,s^{-1}$, respectively, while the $y = ax$ slope, $y = ax + b$ slope and $y = ax + b$ intercept are 1.00, 0.96 and −1.20 $m\,s^{-1}$. Table 5 summarizes the statistical results of the comparison. It should be emphasized that before these comparisons are made, the outlier control is first conducted. The data with HLOS wind differences larger than 1 standard deviation (5.89 $m\,s^{-1}$ for the Mie-cloudy channel and 14.08 $m\,s^{-1}$ for the Rayleigh-clear channel) are removed and are not considered. For Mie-cloudy HLOS wind and Rayleigh-clear HLOS wind, 15 (22.39 %) comparison pairs and 94 (19.54 %) comparison pairs are removed, respectively. Figure 10b and d show statistic histograms of the count comparison between CDL-retrieved HLOS wind and Aeolus Mie-cloudy HLOS wind and between CDL-retrieved HLOS wind and Aeolus Rayleigh-clear HLOS wind.

Additionally, the scatter plots and the statistics histograms of Aeolus Rayleigh-clear HLOS wind against the CDL-retrieved HLOS wind according to the measurements made on ascending and descending tracks are presented individually in Fig. 11. Figure 11a indicates the comparison between the Aeolus ascending measurements against those from CDLs. It is found that the correlation coefficient, the standard deviation, the scaled MAD and the bias are 0.65, 5.83 $m\,s^{-1}$, 4.90 $m\,s^{-1}$ and −0.16 $m\,s^{-1}$, respectively, while the $y = ax$ slope, $y = ax + b$ slope and $y = ax + b$ intercept are 1.02, 1.03 and −0.23 $m\,s^{-1}$. Figure 11c shows the comparison between the Aeolus descending measurements against those from CDLs. The correlation coefficient, the standard deviation, the scaled MAD and the bias are 0.51, 7.47 $m\,s^{-1}$, 6.06 $m\,s^{-1}$ and −2.00 $m\,s^{-1}$, respectively. Besides, the $y = ax$ slope, $y = ax + b$ slope and $y = ax + b$ intercept are 0.97, 0.78 and −2.61 $m\,s^{-1}$. Consequently, the standard deviation, the scaled MAD and the bias on ascending tracks are lower than those on descending tracks. It can especially be found that the significantly negative bias exists in the comparison result of descending HLOS wind and CDL-retrieved HLOS wind. The statistic results are summarized in Table 6. The count comparison histograms of Aeolus Rayleigh ascending and descending HLOS winds against CDL-retrieved HLOS winds are presented in Fig. 11b and d individually.

Since the time period for the comparison of Aeolus and CDL synchronous measurements lasted during 2020, the baselines of the Aeolus product changed accordingly during this period (Rennie et al., 2020). From Baseline 07 to Baseline 08 of the L2B wind product processor, the associated new auxiliary file carrying the parameters needed for the M1 mirror temperature correction was provided but not used in the L2B processing. After the deployment of Baseline 09, the new auxiliary file with the M1 mirror temperature correction parameters was used, thus correcting for the associated biases in the L2B wind product. The bias-corrected dataset consists of Baseline 09 data from 1 to 20 April 2020 and Baseline 10 data from 20 April to 8 October 2020 and the FM-B low-bias reprocessed dataset of 28 June to 31 December 2019. With the Baseline 11 processor deployed, different SNR thresholds for classification of Mie and Rayleigh and an option to transfer Mie SNR results to the Rayleigh channel were added, which allows SNR-based classification to be done for the Rayleigh channel, resulting in a clear quality improvement. Therefore, to evaluate the impact of updating baseline products on the HLOS wind measurements, the Aeolus L2B Rayleigh-clear HLOS wind data from Baselines 07

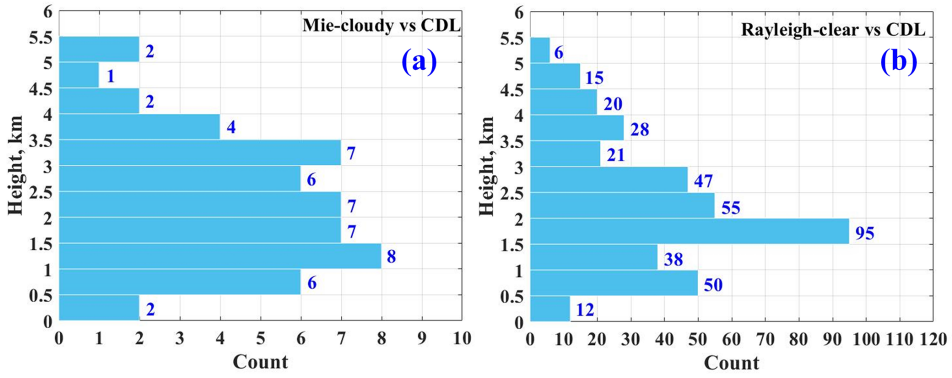

Figure 9. Counts of data pairs at different height ranges of **(a)** Mie-cloudy vs. CDL and **(b)** Rayleigh-clear vs. CDL.

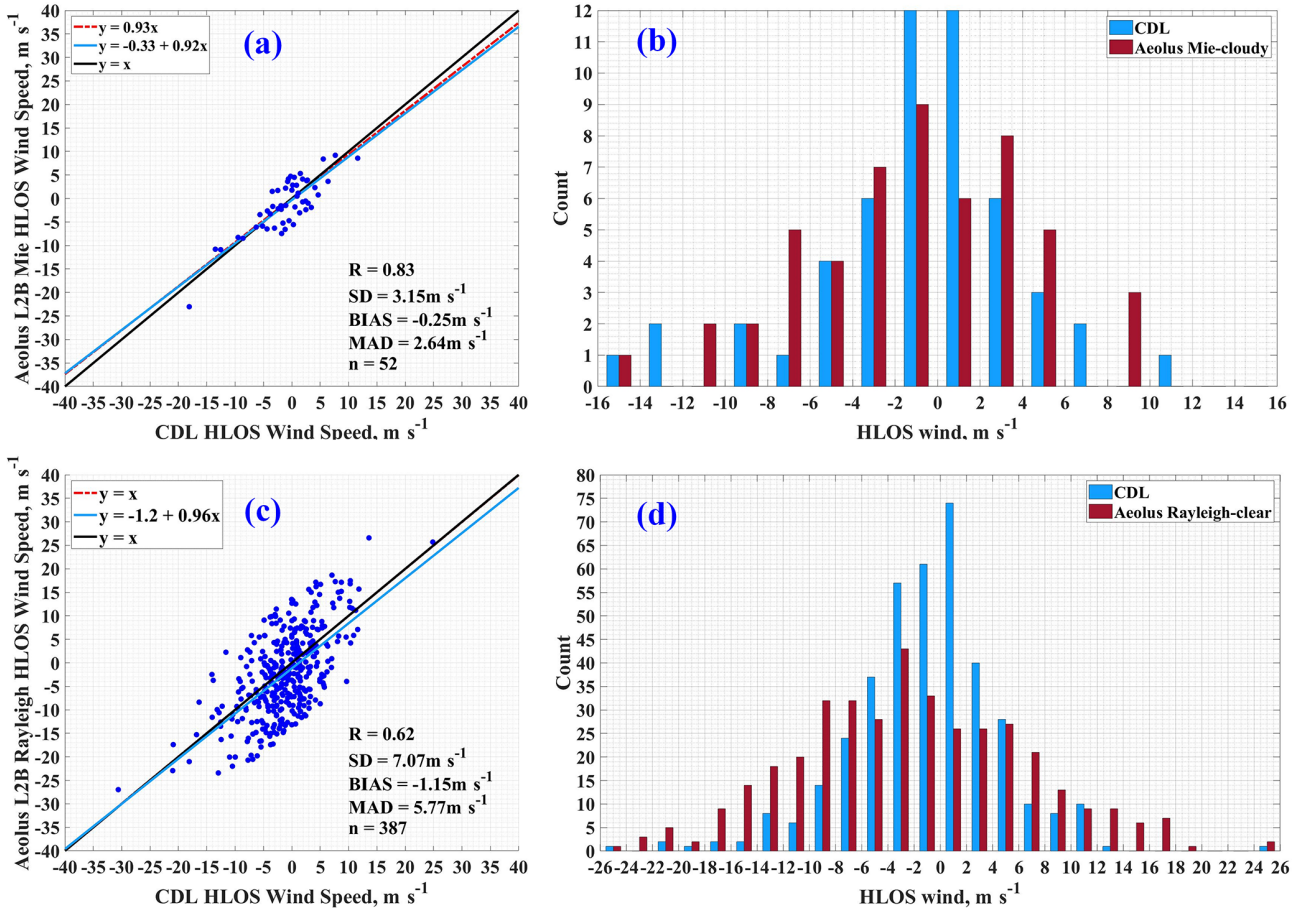

Figure 10. Comparisons of Aeolus L2B Rayleigh-clear HLOS wind velocities and Mie-cloudy HLOS wind velocities against those from CDLs. In panels **(a)** and **(c)**, the dotted red lines represent the $y = ax$ fitting lines, the blue lines represent the $y = ax + b$ fitting lines, and the black lines represent the $y = x$ reference line. Panels **(b)** and **(d)** show the histogram of HLOS wind velocities, where the blue columns represent the count of CDL HLOS wind velocities, and the red columns represent the count of Aeolus HLOS wind velocities.

and 08, Baselines 09 and 10, and Baseline 11 are compared against the CDL-retrieved data individually in Fig. 12a, c and e.

During the comparison period, the Aeolus L2B HLOS wind measurements between January and April 2020 are produced with the Baselines 07 and 08, the measurements between May and September 2020 are with the Baselines 09 and 10, and the rest of the measurements from October 2020 are supported by Baseline 11. In Fig. 12a, the scatter plot for the Aeolus L2B Rayleigh-clear HLOS wind with the Base-

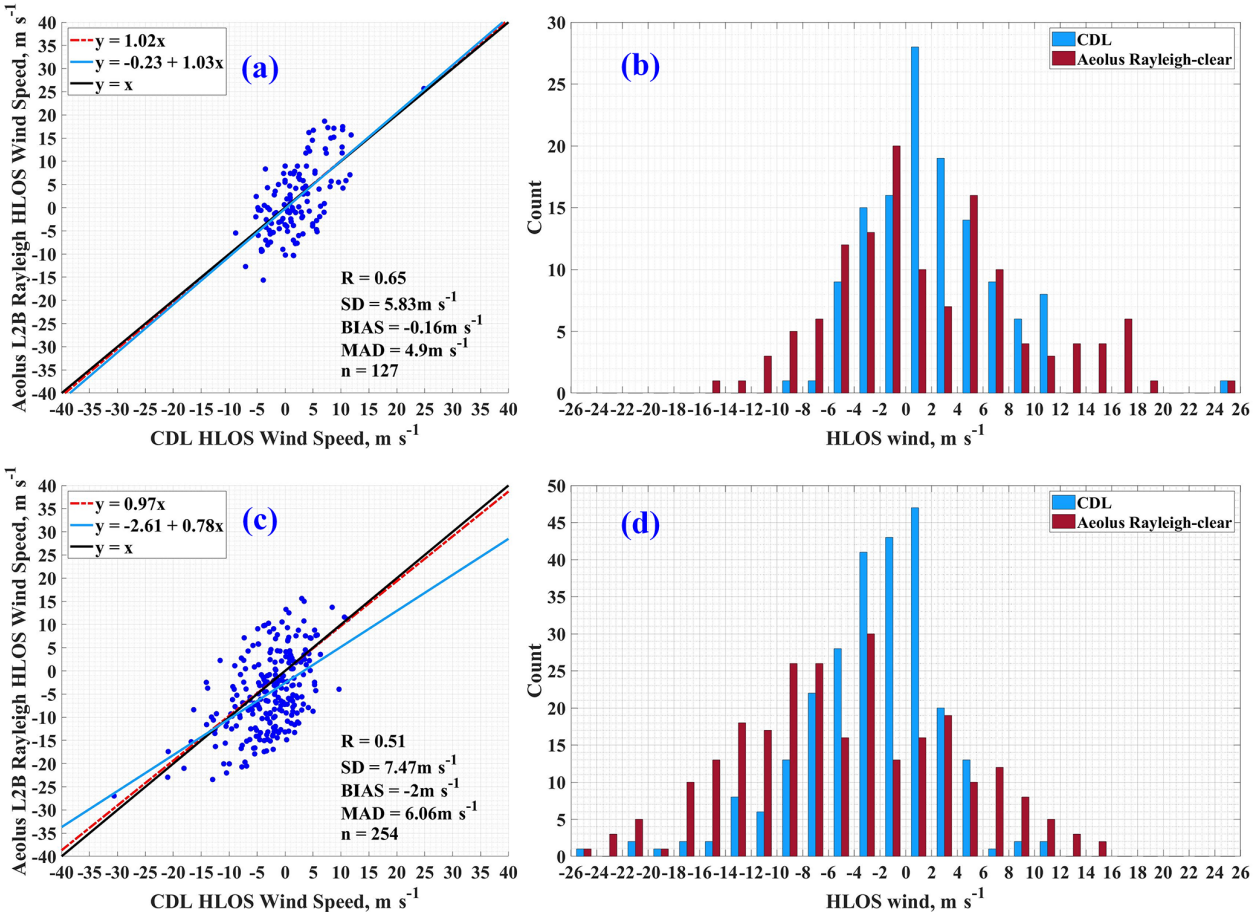

Figure 11. Comparisons of Aeolus Rayleigh-clear HLOS wind against the CDL-retrieved HLOS wind according to the measurements made on **(a, b)** ascending and **(c, d)** descending tracks. The lines and the histograms represent the same as those of Fig. 10.

lines of 07 and 08 is provided, from which it can be found that the correlation coefficient is 0.39, and the standard deviation, the scaled MAD and the bias are 10.20, 8.42 and $-1.23\,\mathrm{m\,s^{-1}}$, respectively. Hence the Aeolus products with Baselines 07 and 08 need to be calibrated further. From the results shown in Fig. 12c and e, thanks to the M1 mirror temperature correction from the Baseline 08 processor to the Baseline 09 processor, the correlation coefficients, the standard deviations, the scaled MAD and the biases are significantly improved compared to those from Baselines 07 and 08. The correlation coefficient reaches 0.75 (0.86) for the scatter plot with Baselines 09 and 10 (Baseline 11). The corresponding standard deviation and scaled MAD decrease to $4.66\,\mathrm{m\,s^{-1}}$ ($4.76\ \mathrm{m\,s^{-1}}$) and $3.84\,\mathrm{m\,s^{-1}}$ ($3.91\,\mathrm{m\,s^{-1}}$), and the bias is suppressed to $-0.98\,\mathrm{m\,s^{-1}}$ ($-0.13\,\mathrm{m\,s^{-1}}$) during the comparison with Baselines 09 and 10 (Baseline 11). The statistical comparison results are also presented in Table 7. From Fig. 12b, d and f, the count histograms of comparison also show the significant improvement of the comparison results from Baselines 07 and 08 to Baselines 09 and 10 and Baseline 11.

Table 7. Statistical comparison of Aeolus Rayleigh HLOS winds of different baselines and CDL-retrieved HLOS winds.

Baselines	07 and 08	09 and 10	11
N points	156	106	100
Correlation	0.39	0.75	0.86
SD ($\mathrm{m\,s^{-1}}$)	10.20	4.66	4.76
Scaled MAD ($\mathrm{m\,s^{-1}}$)	8.42	3.84	3.91
BIAS ($\mathrm{m\,s^{-1}}$)	−1.23	−0.98	−0.13
$y = ax$ slope	1.17	0.99	1.01
$y = ax + b$ slope	1.12	0.97	1.00
$y = ax + b$ intercept ($\mathrm{m\,s^{-1}}$)	−1.16	−1.01	−0.12

5 Discussion

The statistical results in Sect. 4.2 show the inter-comparison consequence of the VAL-OUC campaign of Aeolus and ground-based CDLs. Because of the limited measurement height of CDLs, the HLOS wind data involved in the validation, which are produced by Aeolus and CDLs individu-

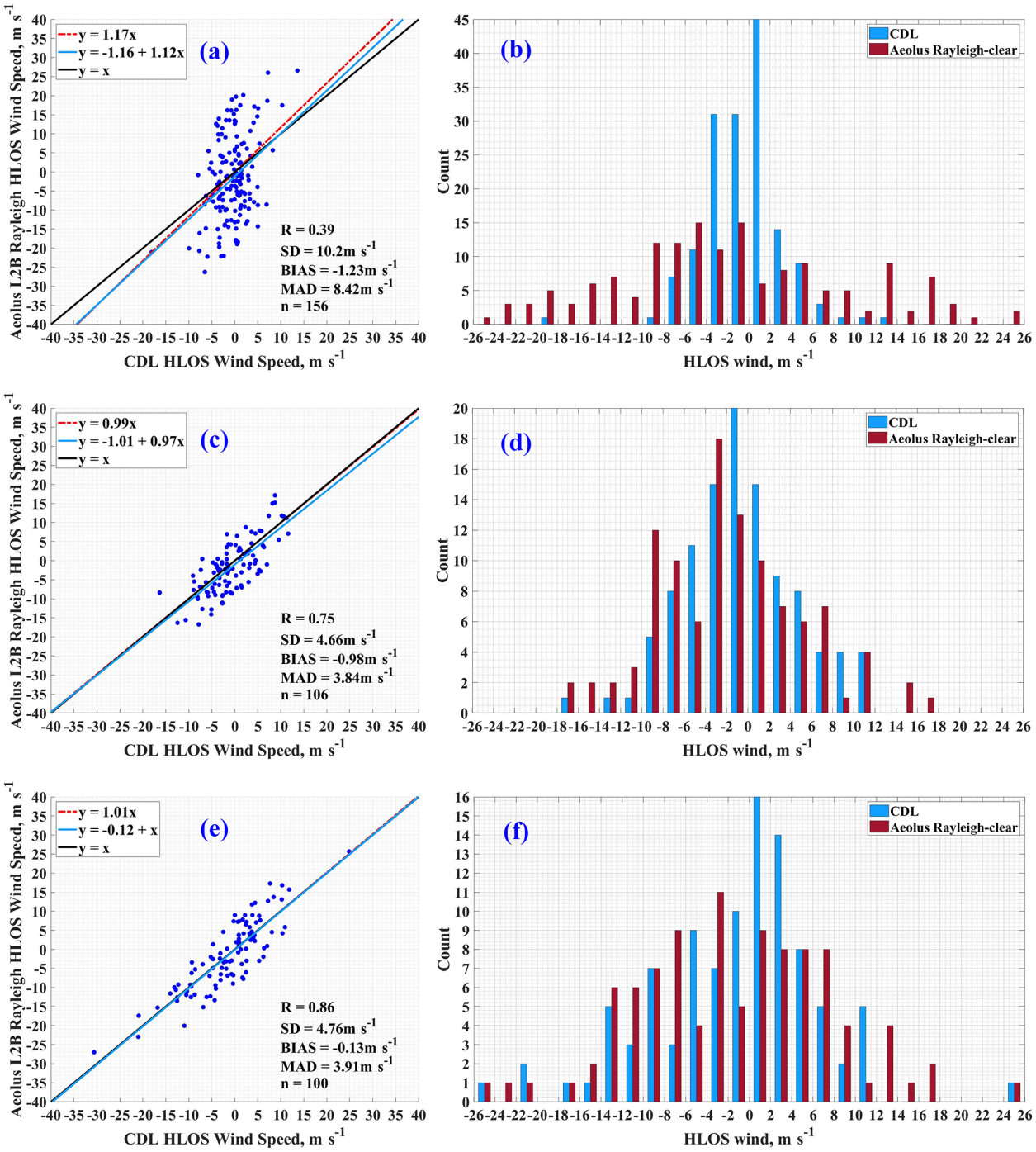

Figure 12. The comparison between the Aeolus L2B Rayleigh HLOS wind data from **(a, b)** Baselines 07 and 08, **(c, d)** Baselines 09 and 10, and **(e, f)** Baseline 11 against the CDL-retrieved HLOS wind data. The lines and the histograms represent the same as those of Fig. 10.

ally, are mainly in the PBL. It is summarized that, for the Rayleigh-clear winds, the correlation coefficient, the standard deviation, the scaled MAD and the bias are 0.62, 7.07 m s^{-1}, 5.77 m s^{-1} and -1.15 m s^{-1}, respectively, while the $y = ax + b$ slope and intercept are 0.96 and -1.20 m s^{-1}. For the Mie-cloudy winds, the correlation coefficient, the standard deviation, the scaled MAD and the bias are 0.83, 3.15 m s^{-1}, 2.64 m s^{-1} and -0.25 m s^{-1}, while the $y = ax + b$ slope and intercept are 0.92 and -0.33 m s^{-1}.

Additionally, we summarized the recent comparison campaigns from the Cal/Val teams all over the world. The corresponding comparison results are also presented in Table 8a

Table 8. Summary of the recent comparison campaign validation results: **(a)** Rayleigh-clear, **(b)** Mie-cloudy.

(a) Rayleigh-clear							
Campaigns and instruments		*R*	SD, $m\,s^{-1}$	Scaled MAD, $m\,s^{-1}$	Bias, $m\,s^{-1}$	Slope	Intercept, $m\,s^{-1}$
VAL-OUC (this study)		0.62	7.07	5.77	−1.15	0.96	−1.20
WindVal III/A2D (Lux et al., 2020a)		0.80	3.6	3.6	2.6	–	–
WindVal III/2 µm DWL (Witschas et al., 2020)		0.95	4.75	3.97	2.11	0.99	2.23
AVATARE (Witschas et al., 2020)		0.76	5.27	4.36	−4.58	0.98	−4.39
AboVE-OHP (Khaykin et al., 2020)		0.96	3.2	–	1.5	–	–
RV *Polarstern* cruise PS116 (Baars et al., 2020)		–	–	4.84	1.52	0.97	1.57
MARA (Belova et al., 2021)	In summer	0.82	5.8	–	0.0	1.1	0.0
	In winter	0.81	5.6	–	−1.3	0.87	−0.8
ESRAD (Belova et al., 2021)	In summer	0.92	4.5	–	−0.4	1.0	−0.5
	In winter	0.88	5.2	–	−0.4	1.0	−0.6
WPR over Japan (Iwai et al., 2021)	Baseline 2B02	0.95	8.08	7.35	1.69	0.98	1.75
	Baseline 2B10	0.90	7.89	7.08	−0.82	0.94	−0.74
CDWL in Kobe (Iwai et al., 2021)	Baseline 2B02	0.98	6.17	4.92	0.46	1.05	0.61
	Baseline 2B10	0.96	5.69	5.21	−0.81	0.98	−0.88
CDWL in Okinawa (Iwai et al., 2021)	Baseline 2B02	0.93	6.57	5.68	1.08	0.99	1.07
	Baseline 2B10	0.79	6.53	5.58	−0.48	1.03	−0.52
GPS-RS in Okinawa (Iwai et al., 2021)	Baseline 2B02	0.99	4.55	4.77	1.00	0.99	1.00
	Baseline 2B10	0.99	4.43	3.97	0.45	1.01	0.38
RWP network over China (Guo et al., 2021b)		0.94	4.2	–	−0.28	1.01	−0.41
(b) Mie-cloudy							
Campaigns and instruments		*R*	SD, $m\,s^{-1}$	Scaled MAD, $m\,s^{-1}$	Bias, $m\,s^{-1}$	Slope	Intercept, $m\,s^{-1}$
VAL-OUC (this study)		0.83	3.15	2.64	−0.25	0.92	−0.33
WindVal III/A2D (Lux et al., 2020a)		–	–	–	–	–	–
WindVal III/2 µm DWL (Witschas et al., 2020)		0.92	2.95	2.24	2.26	0.96	2.7
AVATARE (Witschas et al., 2020)		0.91	3.02	2.22	−0.17	1.01	−0.21
AboVE-OHP (Khaykin et al., 2020)		–	–	–	–	–	–
RV *Polarstern* cruise PS116 (Baars et al., 2020)		–	–	1.58	0.95	0.95	1.13
MARA (Belova et al., 2021)	In summer	0.63 (ascend); 0.72 (descend)	6.8 (ascend); 6.5 (descend)	–	6.6 (ascend); −0.5 (descend)	1.0 (ascend); 1.3 (descend)	6.5 (ascend); −2.4 (descend)
	In winter	0.73 (ascend); 0.70 (descend)	5.7 (ascend); 5.6 (descend)	–	−1.0 (ascend); 0.9 (descend)	1.1 (ascend); 1.2 (descend)	0.4 (ascend); −1.2 (descend)
ESRAD (Belova et al., 2021)	In summer	0.76 (ascend); 0.90 (descend)	4.7 (ascend); 5.5 (descend)	–	0.5 (ascend); 0.7 (descend)	0.8 (ascend); 0.8 (descend)	0.5 (ascend); 0.2 (descend)
	In winter	0.91 (ascend); 0.85 (descend)	3.9 (ascend); 5.2 (descend)	–	2.4 (ascend); 0.9 (descend)	1.0 (ascend); 0.9 (descend)	2.3 (ascend); 0.5 (descend)
WPR over Japan (Iwai et al., 2021)	Baseline 2B02	0.95	6.83	5.94	2.42	0.98	2.44
	Baseline 2B10	0.93	6.47	5.66	−0.51	0.96	−0.44
CDWL in Kobe (Iwai et al., 2021)	Baseline 2B02	0.98	4.80	3.55	1.63	1.05	1.76
	Baseline 2B10	0.97	5.15	3.92	0.16	1.02	0.22
CDWL in Okinawa (Iwai et al., 2021)	Baseline 2B02	0.97	3.64	3.76	2.38	1.01	2.37
	Baseline 2B10	0.86	4.74	3.86	−0.26	0.86	−0.04
GPS-RS in Okinawa (Iwai et al., 2021)	Baseline 2B02	0.97	4.52	4.14	2.15	0.97	2.07
	Baseline 2B10	0.95	5.81	3.99	−0.71	0.92	−0.22
RWP network over China (Guo et al., 2021b)		0.81	6.82	–	−0.64	0.99	−0.67

and b. From Table 8, the statistical parameters including correlation coefficient, SD, MAD, bias, slope and intercept of recent calibration and validation campaigns show consistent tendency and similar comparison results. The deviations among all of these studies may result from the differences in operation strategies, spatial distances and temporal gaps. In summary, considering that this study conducts the inter-comparison with the data pairs mainly in the heterogeneous atmospheric boundary layer, the statistical results of this study are reasonable and significant due to the long time period and large number of ground sites included for the comparison over China.

6 Summary and conclusion

To evaluate the accuracy and precision of the Aeolus-retrieved wind results, ground-based coherent Doppler wind lidars were deployed at 17 observation stations over China for simultaneous measurements under the framework of the VAL-OUC campaign from January to December 2020. To ensure the quality of the measurement data from CDLs, only wind observations with SNR > -10 dB are utilized. Mie-cloudy and Rayleigh-clear wind velocities from the Aeolus L2B are selected with the corresponding "validity_flag" of TRUE with estimated errors lower than 4 and 8 m s^{-1}, respectively. Moreover, the Aeolus lowest-atmospheric-range bins close to the ground are removed from the comparison. In this study, the horizontal distance between the locations of CDLs and the Aeolus footprints must be less than 80 km. Since the CDLs provide continuous atmospheric observations with a temporal resolution of 1 min, there is no time difference between CDL and simultaneous Aeolus measurements. Vertical averaging of the CDL-produced wind measurements over Aeolus range bins is performed. Overall, after the strict quality control introduced above, 52 simultaneous Mie-cloudy comparison pairs and 387 Rayleigh-clear comparison pairs from this campaign are acquired.

Using the simultaneous wind measurements with CDLs and Aeolus, the Rayleigh-clear HLOS wind velocities and Mie-cloudy HLOS wind velocities from Aeolus are compared with those from CDLs, respectively. All of the Aeolus-produced L2B Mie-cloudy HLOS wind, Rayleigh-clear HLOS wind and CDL-produced HLOS wind are compared individually. A total of 52 measurement cases for Mie-cloudy winds could be identified for the comparison. From this statistical result, the correlation coefficient, the standard deviation, the scaled MAD and the bias are 0.83, 3.15 m s^{-1}, 2.64 m s^{-1} and -0.25 m s^{-1}, respectively, while the $y = ax$ slope, the $y = ax + b$ slope and the $y = ax + b$ intercept are 0.93, 0.92 and -0.33 m s^{-1}. For Aeolus L2B Rayleigh-clear HLOS wind and CDL HLOS wind data, 387 valid observations could be used for the comparison. Accordingly, the correlation coefficient, the standard deviation, the scaled MAD and the bias are 0.62, 7.07 m s^{-1}, 5.77 m s^{-1} and -1.15 m s^{-1}, respectively, while the $y = ax$ slope, the $y = ax + b$ slope and the $y = ax + b$ intercept are 1.00, 0.96 and -1.20 m s^{-1}. Besides, the scatter diagrams and the count histogram of Aeolus Rayleigh-clear HLOS wind according to the measurements made on ascending and descending tracks against the synchronous CDL-retrieved HLOS wind are plotted individually. It is found that the standard deviation and bias on ascending tracks are lower than those on descending tracks. The significantly negative bias especially exists in the Aeolus Rayleigh-clear descending HLOS wind comparison results. Moreover, to evaluate the accuracy of Aeolus HLOS wind measurements with the baseline update, the Aeolus L2B Mie-cloudy and Rayleigh-clear HLOS wind data under Baselines 07 and 08, Baselines 09 and 10, and Baseline 11 are compared against the CDL-retrieved HLOS wind data, respectively. From the comparison results, marked misfits between the wind data from Aeolus Baselines 07 and 08 and wind data from CDLs in the atmospheric boundary layers and the lower troposphere are found. After that, the M1 mirror temperature bias correction processor was deployed, and new Rayleigh channel thresholds were added, resulting in the significant improvement in the performances of Aeolus wind measurements under Baselines 09, 10 and 11. It has to be emphasized that the misfit may result from the contamination of the Mie backscatter signal from the Rayleigh backscatter signal, which introduces errors to the retrieval of Rayleigh-clear HLOS wind velocity. Additionally, the distance between the CDL sites and the footprint of Aeolus and the strong small-scale dynamics field may cause differences. Finally, the statistical results of recent Aeolus wind product calibration and validation campaigns that have been reported so far are summarized and compared. It is figured out that this study acquired similar results compared with other recent inter-comparison campaigns, and all the comparison results show a consistent tendency.

In the atmospheric boundary layer and the lower troposphere, the vertical velocity from convection and turbulence could influence the comparison due to the impact of vertical velocity on the HLOS wind velocity retrieval from Aeolus. Hence, a method is described to use the vertical velocity measured with the CDLs to project onto the Aeolus LOS direction and consider it for the comparison.

Data availability. The Aeolus data are downloaded via the website https://aeolus-ds.eo.esa.int/oads/access/collection (last access: 23 August 2021) (ESA, 2021). The presented work includes preliminary data (not fully calibrated or validated and not yet publicly released) of the Aeolus mission, which is part of the European Space Agency (ESA) Earth Explorer programme. This includes wind products from before the public data release in May 2020 and/or aerosol and cloud products, which have not yet been publicly released. The preliminary Aeolus wind products will be reprocessed during 2020 and 2021 and will include in particular a significant L2B product wind bias reduction and improved L2A radiometric calibration. Aerosol and cloud products became publicly avail-

able on 12 July 2021. The processor development, improvement and product reprocessing preparation are performed by the Aeolus DISC (Data, Innovation and Science Cluster), which involves DLR, DoRIT, ECMWF, KNMI, CNRS, S&T, ABB and Serco, in close cooperation with the Aeolus PDGS (Payload Data Ground Segment). The analysis has been performed in the framework of the Aeolus Scientific Calibration and Validation Team (ACVT). To get the CDL data please contact Songhua Wu (wush@ouc.edu.cn) at the Ocean University of China.

Author contributions. SW contributed to the study design for inter-comparison of wind measurement with Aeolus and ground-based coherent Doppler lidar in the PBL over China. KS, GD, SW and OR contributed to the data analyses. GD and KS wrote the manuscript. XiaW, XL, BL and XS helped in programming. KS downloaded the Aeolus data. RL, JY and XitW prepared and operated the CDLs. All the co-authors discussed the results and reviewed the manuscript.

Competing interests. The contact author has declared that neither they nor their co-authors have any competing interests.

Disclaimer. Publisher's note: Copernicus Publications remains neutral with regard to jurisdictional claims in published maps and institutional affiliations.

Special issue statement. This article is part of the special issue "Aeolus data and their application (AMT/ACP/WCD inter-journal SI)". It is not associated with a conference.

Acknowledgements. We thank our colleagues including Xiaomin Chen, Qichao Wang and Xiangying E from Ocean University of China (OUC) for the discussion and the suggestion during the data analyses; Dahai Wang from Qingdao Leice Transient Technology Co., Ltd. for preparing and operating the CDLs. We also thank the Aeolus Cal/Val teams who gave advice on this work during the workshop of Aeolus. This work was also supported by the Dragon 4 and Dragon 5 programmes, which were conducted by the European Space Agency (ESA) and the National Remote Sensing Center of China (NRSCC) under grants 32296 and 59089.

Financial support. This research has been supported by the National Key Research and Development Program of China (grant no. 2019YFC1408001), the Key Technology Research and Development Program of Shandong (grant no. 2019GHZ023), and the National Natural Science Foundation of China (grant nos. 61975191 and 41905022).

Review statement. This paper was edited by Ad Stoffelen and reviewed by two anonymous referees.

References

Baars, H., Herzog, A., Heese, B., Ohneiser, K., Hanbuch, K., Hofer, J., Yin, Z., Engelmann, R., and Wandinger, U.: Validation of Aeolus wind products above the Atlantic Ocean, Atmos. Meas. Tech., 13, 6007–6024, https://doi.org/10.5194/amt-13-6007-2020, 2020.

Bedka, K. M., Nehrir, A. R., Kavaya, M., Barton-Grimley, R., Beaubien, M., Carroll, B., Collins, J., Cooney, J., Emmitt, G. D., Greco, S., Kooi, S., Lee, T., Liu, Z., Rodier, S., and Skofronick-Jackson, G.: Airborne lidar observations of wind, water vapor, and aerosol profiles during the NASA Aeolus calibration and validation (Cal/Val) test flight campaign, Atmos. Meas. Tech., 14, 4305–4334, https://doi.org/10.5194/amt-14-4305-2021, 2021.

Belova, E., Kirkwood, S., Voelger, P., Chatterjee, S., Satheesan, K., Hagelin, S., Lindskog, M., and Körnich, H.: Validation of Aeolus winds using ground-based radars in Antarctica and in northern Sweden, Atmos. Meas. Tech., 14, 5415–5428, https://doi.org/10.5194/amt-14-5415-2021, 2021.

Chanin, M., Garnier, A., Hauchecorne, A., and Porteneuve, J.: A Doppler lidar for measuring winds in the middle atmosphere, Geophys. Res. Lett., 16, 1273–1276, 1989.

ESA: The four candidate Earth Explorer core missions – Atmospheric Dynamics Mission, ESA Report for Mission Selection ESA SP-1233, Noordwijk, the Netherlands, 145 pp., 1999.

ESA: ADM-Aeolus Science Report, ESA SP-1311, Noordwijk, the Netherlands, 121 pp., 2008.

ESA: ESA Aeolus Online Dissemination System, ESA [data set], available at: https://aeolus-ds.eo.esa.int/oads/access/collection, last access: 23 August 2021.

Flesia, C. and Korb, C. L.: Theory of the double-edge molecular technique for Doppler lidar wind measurement, Appl. Optics, 38, 432–440, 1999.

Guo, J., Zhang, J., Yang, K., Liao, H., Zhang, S., Huang, K., Lv, Y., Shao, J., Yu, T., Tong, B., Li, J., Su, T., Yim, S. H. L., Stoffelen, A., Zhai, P., and Xu, X.: Investigation of near-global daytime boundary layer height using high-resolution radiosondes: first results and comparison with ERA5, MERRA-2, JRA-55, and NCEP-2 reanalyses, Atmos. Chem. Phys., 21, 17079–17097, https://doi.org/10.5194/acp-21-17079-2021, 2021a.

Guo, J., Liu, B., Gong, W., Shi, L., Zhang, Y., Ma, Y., Zhang, J., Chen, T., Bai, K., Stoffelen, A., de Leeuw, G., and Xu, X.: Technical note: First comparison of wind observations from ESA's satellite mission Aeolus and ground-based radar wind profiler network of China, Atmos. Chem. Phys., 21, 2945–2958, https://doi.org/10.5194/acp-21-2945-2021, 2021b.

IEC: Wind turbines – Part 12-1: Power performance measurements of electricity producing wind turbines, IEC 61400-12-1, Edition 2 Committee Draft, Geneva, Switzerland, 2011.

Iwai, H., Aoki, M., Oshiro, M., and Ishii, S.: Validation of Aeolus Level 2B wind products using wind profilers, ground-based Doppler wind lidars, and radiosondes in Japan, Atmos. Meas. Tech., 14, 7255–7275, https://doi.org/10.5194/amt-14-7255-2021, 2021.

Kanitz, T., Lochard, J., Marshall, J., McGoldrick, P., Lecrenier, O., Bravetti, P., Reitebuch, O., Rennie, M., Wernham, D., and Elfving, A.: Aeolus first light: first glimpse, International Conference on Space Optics – ICSO 2018, Crete, Greece, 9–12 October 2018, 111801R, 2018.

Khaykin, S. M., Hauchecorne, A., Wing, R., Keckhut, P., Godin-Beekmann, S., Porteneuve, J., Mariscal, J.-F., and Schmitt, J.: Doppler lidar at Observatoire de Haute-Provence for wind profiling up to 75 km altitude: performance evaluation and observations, Atmos. Meas. Tech., 13, 1501–1516, https://doi.org/10.5194/amt-13-1501-2020, 2020.

Lux, O., Lemmerz, C., Weiler, F., Marksteiner, U., Witschas, B., Rahm, S., Geiß, A., and Reitebuch, O.: Intercomparison of wind observations from the European Space Agency's Aeolus satellite mission and the ALADIN Airborne Demonstrator, Atmos. Meas. Tech., 13, 2075–2097, https://doi.org/10.5194/amt-13-2075-2020, 2020a.

Lux, O., Wernham, D., Bravetti, P., McGoldrick, P., Lecrenier, O., Riede, W., D'Ottavi, A., Sanctis, V. de, Schillinger, M., Lochard, J., Marshall, J., Lemmerz, C., Weiler, F., Mondin, L., Ciapponi, A., Kanitz, T., Elfving, A., Parrinello, T., and Reitebuch, O.: High-power and frequency-stable ultraviolet laser performance in space for the wind lidar on Aeolus, Opt. Lett., 45, 1443–1446, https://doi.org/10.1364/OL.387728, 2020b.

Marksteiner, U.: Airborne Lidar Observations for the validation of the ADM-Aeolus instrument, PhD Thesis, Technical University of Munich, available at: http://mediatum.ub.tum.de/doc/1136781/1136781.pdf (last access: 23 August 2021), 2013.

Martin, A., Weissmann, M., Reitebuch, O., Rennie, M., Geiß, A., and Cress, A.: Validation of Aeolus winds using radiosonde observations and numerical weather prediction model equivalents, Atmos. Meas. Tech., 14, 2167–2183, https://doi.org/10.5194/amt-14-2167-2021, 2021.

McKay, J. A.: Assessment of a multibeam Fizeau wedge interferometer for Doppler wind lidar, Appl. Optics, 41, 1760–1767, 2002.

Reitebuch, O.: The spaceborne wind lidar mission ADM-Aeolus, in: Atmospheric Physics, Springer, Berlin, Heidelberg, 815–827, 2012.

Reitebuch, O., Lemmerz, C., Nagel, E., Paffrath, U., Durand, Y., Endemann, M., Fabre, F., and Chaloupy, M.: The airborne demonstrator for the direct-detection Doppler wind lidar ALADIN on ADM-Aeolus. Part I: Instrument design and comparison to satellite instrument, J. Atmos. Ocean. Tech., 26, 2501–2515, 2009.

Reitebuch, O., Lemmerz, C., Lux, O., Marksteiner, U., Rahm, S., Weiler, F., Witschas, B., Meringer, M., Schmidt, K., Huber, D., Nikolaus, I., Geiss, A., Vaughan, M., Dabas, A., Flament, T., Stieglitz, H., Isaksen, L., Rennie, M., Kloe, J. D., Marseille, G.-J., Stoffelen, A., Wernham, D., Kanitz, T., Straume, A.-G., Fehr, T., Bismarck, J. von, Floberghagen, R., and Parrinello, T.: Initial Assessment of the Performance of the First Wind Lidar in Space on Aeolus, EPJ Web Conf., 237, 1010, https://doi.org/10.1051/epjconf/202023701010, 2020.

Rennie, M. and Isaksen, L.: The NWP impact of Aeolus Level-2B winds at ECMWF, Technical Memorandum, ECMWF, https://doi.org/10.21957/alift7mhr, 2020.

Rennie, M., Tan, D., Andersson, E., Poli, P., Dabas, A., De Kloe, J., Marseille, G.-J., and Stoffelen, A.: Aeolus Level-2B Algorithm Theoretical Basis Document (Mathematical Description of the Aeolus L2B Processor), ESA, AED-SD-ECMWF-1025 L2B-038, V. 3.4, 124 pp., available at: https://earth.esa.int/eogateway/missions/aeolus/data (last access: 25 January 2021), 2020.

Stoffelen, A., Pailleux, J., Källén, E., Vaughan, J. M., Isaksen, L., Flamant, P., Wergen, W., Andersson, E., Schyberg, H., Culoma, A., Meynart, R., Endemann, M., and Ingmann, P.: The Atmospheric Dynamics Mission for Global Wind Field Measurement, B. Am. Meteorol. Soc., 86, 73–88, https://doi.org/10.1175/BAMS-86-1-73, 2005.

Straume, A. G., Elfving, A., Wernham, D., de Bruin, F., Kanitz, T., Schuettemeyer, D., von Bismarck, J., Buscaglione, F., Lecrenier, O., and McGoldrick, P.: ESA's spaceborne lidar mission ADM-Aeolus; project status and preparations for launch, EPJ Web Conf., 176, 04007, https://doi.org/10.1051/epjconf/201817604007, 2018.

Tan, D. G., Andersson, E., Kloe, J. D., Marseille, G.-J., Stoffelen, A., Poli, P., Denneulin, M.-L., Dabas, A., Huber, D., and Reitebuch, O.: The ADM-Aeolus wind retrieval algorithms, Tellus A, 60, 191–205, 2008.

Weiler, F., Rennie, M., Kanitz, T., Isaksen, L., Checa, E., de Kloe, J., Okunde, N., and Reitebuch, O.: Correction of wind bias for the lidar on board Aeolus using telescope temperatures, Atmos. Meas. Tech., 14, 7167–7185, https://doi.org/10.5194/amt-14-7167-2021, 2021.

Witschas, B., Lemmerz, C., Geiß, A., Lux, O., Marksteiner, U., Rahm, S., Reitebuch, O., and Weiler, F.: First validation of Aeolus wind observations by airborne Doppler wind lidar measurements, Atmos. Meas. Tech., 13, 2381–2396, https://doi.org/10.5194/amt-13-2381-2020, 2020.

Wu, S., Liu, B., Liu, J., Zhai, X., Feng, C., Wang, G., Zhang, H., Yin, J., Wang, X., and Li, R.: Wind turbine wake visualization and characteristics analysis by Doppler lidar, Opt. Express, 24, A762–A780, 2016.

Zhang, Y., Sun, K., Gao, Z., Pan, Z., Shook, M. A., and Li, D.: Diurnal climatology of planetary boundary layer height over the contiguous United States derived from AMDAR and reanalysis data, J. Geophys. Res.-Atmos., 125, e2020JD032803, https://doi.org/10.1029/2020JD032803, 2020.